The Journal of Chemical Physics ARTICLE pubs.aip.org/aip/jcp

Capillary filling of star polymer melts in nanopores

Cite as: J. Chem. Phys. 160, 054903 (2024); doi: 10.1063/5.0188955
Submitted: 25 November 2023 • Accepted: 15 January 2024 •
Published Online: 6 February 2024

Jianwei Zhang,[1] Jinyu Lei,[1] Pu Feng,[2] George Floudas,[3,4,5] Guangzhao Zhang,[1,a)] and Jiajia Zhou[6,7,a)]

AFFILIATIONS

[1] Faculty of Materials Science and Engineering, South China University of Technology, Guangzhou 510640, China
[2] School of Civil Engineering and Transportation, South China University of Technology, Guangzhou 510640, China
[3] Max Planck Institute for Polymer Research, 55128 Mainz, Germany
[4] Department of Physics, University of Ioannina, 45110 Ioannina, Greece
[5] Institute of Materials Science and Computing, University Research Center of Ioannina (URCI), 45110 Ioannina, Greece
[6] South China Advanced Institute for Soft Matter Science and Technology, School of Emergent Soft Matter, South China University of Technology, Guangzhou 510640, China
[7] Guangdong Provincial Key Laboratory of Functional and Intelligent Hybrid Materials and Devices, South China University of Technology, Guangzhou 510640, China

Note: This paper is part of the JCP Special Topic on Polymer Nanoconfinement.
[a)]**Authors to whom correspondence should be addressed:** msgzzhang@scut.edu.cn and zhouj2@scut.edu.cn

ABSTRACT

The topology of a polymer profoundly influences its behavior. However, its effect on imbibition dynamics remains poorly understood. In the present work, capillary filling (during imbibition and following full imbibition) of star polymer melts was investigated by molecular dynamics simulations with a coarse-grained model. The reversal of imbibition dynamics observed for linear-chain systems was also present for star polymers. Star polymers with short arms penetrate slower than the prediction of the Lucas–Washburn equation, while systems with long arms penetrate faster. The radius of gyration increases during confined flow, indicating the orientation and disentanglement of arms. In addition, the higher the functionality of the star polymer, the more entanglement points are retained. Besides, a stiff region near the core segments of the stars is observed, which increases in size with functionality. The proportion of different configurations of the arms (e.g., loops, trains, tails) changes dramatically with the arm length and degree of confinement but is only influenced by the functionality when the arms are short. Following full imbibition, the different decay rates of the self-correlation function of the core-to-end vector illustrate that arms take a longer time to reach the equilibrium state as the functionality, arm length, and degree of confinement increase, in agreement with recent experimental findings. Furthermore, the star topology induces a stronger effect of adsorption and friction, which becomes more pronounced with increasing functionality.

I. INTRODUCTION

Recently, star polymers have attracted increasing attention due to their unique molecular topology linked to several emerging applications.[1,2] One example is their infiltration into narrow pores with a size comparable to the polymer size, which is of fundamental interest for application in nanofluidics and membranes.[3–6] Chains under this kind of spatial confinement exhibit nonclassical behavior with respect to their viscosity,[7] mobility,[8] entanglements,[9] etc. The imbibition dynamics of linear chains on this scale also shows deviations from the classical prediction of the Lucas–Washburn equation (LWE),[10,11]

$$h(t) = \sqrt{\frac{\gamma R \cos\theta}{2\eta} t}, \tag{1}$$

where $h(t)$ is the filling length of fluid inside the pore and is a function of wetting time t, γ is the surface tension, R is the radius of a

cylindrical capillary, θ is the equilibrium contact angle of fluid on the capillary wall, and η is the bulk viscosity. Shorter chain polymers exhibit slower imbibition dynamics than predicted by theory when there is no entanglement or just a few entanglements.[12] When the chain length surpasses a certain threshold, the dynamics within the same nanopores reverses, and faster-than-prediction imbibition emerges.[13,14] The phenomenon is not only observed inside regular-shaped capillaries but also within irregular shaped nano-channels in dense packings of nanoparticles. Providing a fundamental understanding of this phenomenon is closely linked with the applications of porous materials with polymer fillers.[15–17]

Recent works have explained the physics behind this phenomenon. The strong interaction between polymer chains and the capillary walls induces a layer of adsorbed chains, which is termed the "dead zone."[18] On the macroscopic level, the capillary radius is larger than the size of polymer chains, and the thickness of the adsorption layer can be neglected. However, this layer significantly decreases the effective radius of nanopores in small capillaries. In addition, the free energy of chains under confinement increases.[18] The combination of these factors results in slower capillary filling than theoretically predicted. Faster imbibition occurs when polymer chains are well entangled. Under confinement, chains are constrained by other chains and can only move along the "reptation tube" so that the chain's mobility is enhanced.[18,19] This effect leads to chain disentanglement during flow, which further results in a reduced effective viscosity. As expected, a higher degree of confinement brings about more pronounced effects.[19–21] The change in the interfacial friction or slippage of the polymer-wall interface should also be valued in certain cases.[20,22] Besides the imbibition dynamics, a better understanding of chain dynamics in nanopores is also necessary. In previous studies by dielectric spectroscopy, the configuration transition of chains from the free one to the fixed one (e.g., loop or train) led to a piecewise evolution of the dielectric loss curves corresponding to the chain modes.[23] This process also induces extremely slow adsorption kinetics, which is more distinct under higher degrees of confinement.[24]

Although the imbibition dynamics have been studied in detail for linear polymers, little is known of how the change in polymer topology influences both the imbibition dynamics and chain dynamics under nanometer confinement. For example, is the mechanism of adsorption sensitive to the polymer architecture? Going one step further, could one employ the imbibition process in nanopores as a means of separating different chain topologies in perfectly miscible polymer blends, e.g., star from linear polymer chains?

Compared with linear chains, star polymers have significantly different dynamics in their bulk state.[25] The simplest star polymer consists of multiple linear chains of the same length grafted onto a core. Even in this case, the basic characteristics of the polymer, such as the chain relaxation or the glass temperature, cannot be described completely by classic models or scaling laws.[26,27] The adsorption kinetics of star polymer at an interface should also be modified by its multi-end topology.[28–30] In addition, much effort has been devoted to finding the relation between the fundamental properties of star polymers and their architecture (i.e., functionality f and molecular weight M).[31–34] However, it remains to be explored whether these theories can predict behavior under extreme spatial restrictions.

In this work, we employ extensive molecular dynamics simulations of the capillary filling of a series of star polymer melts in nanopores. The whole filling process is divided into two stages: (i) during imbibition, and (ii) after full imbibition. Our research focuses on both the imbibition dynamics and the chain dynamics under confinement. During imbibition, our aim is two-fold. First, to predict the penetration length of star polymers in comparison to the classical Lucas–Washburn equation, and second, to understand the chain behavior (e.g., chain configuration, orientation, disentanglement, and chain mobility) during filling. Following the full imbibition, our objective is to investigate the relaxation of star polymers as a function of pore size, functionality, and arm molecular weight and to evaluate their ability to reach a steady state. Perhaps unsurprisingly, we find that multi-arm stars behave dynamically different under confinement with respect to linear polymers confined in the same nanopores.

II. SIMULATION MODEL AND DETAILS

We studied the imbibition dynamics of star polymer melts by performing coarse-grained molecular dynamics simulations. The polymer chains are presented by the bead–spring model and the capillary wall is modeled as ordered spherical beads. Non-bonded interactions between all beads were modeled by the truncated-shifted Lennard-Jones (LJ) potential,[35]

$$U_{LJ}(r) = \begin{cases} 4\varepsilon_{LJ}\left[\left(\frac{\sigma}{r_{ij}}\right)^{12} - \left(\frac{\sigma}{r_{ij}}\right)^{6} - \left(\frac{\sigma}{r_{cut}}\right)^{12} + \left(\frac{\sigma}{r_{cut}}\right)^{6}\right], & r_{ij} \le r_{cut}, \\ 0, & r_{ij} > r_{cut}, \end{cases} \tag{2}$$

where σ is the bead diameter, ε_{LJ} is the Lennard-Jones interaction parameter, r_{ij} is the distance between the ith and jth beads, and the cutoff distance r_{cut} was set to 2.5σ. For interactions between polymer beads, we set $\varepsilon_{LJ} = 1.4k_BT$ and $\sigma = 1.0$, where k_B is the Boltzmann constant and T is the temperature. The bonds connecting beads to polymer chains were modeled by the finite extension nonlinear elastic (FENE) potential[36]

$$U_{FENE}(r) = -\frac{1}{2}k_{spring}{R_{\max}}^2 \ln\left(1 - \frac{r^2}{{R_{\max}}^2}\right), \tag{3}$$

with the spring constant $k_{spring} = 30k_BT/\sigma^2$ and the maximum bond length $R_{\max} = 1.5\sigma$. Herein, we studied star polymers with three different degrees of polymerization of arms (N_{arm} = 10, 50, and 100) and four different numbers of arms (f = 2, 4, 6, and 12), thus 12 types of polymers in total. The system codes and details are listed in Table I. The data for the radius of gyration in the table were calculated in the bulk of static equilibrium states (the details will be discussed later).

Cylindrical nanopores with length $L = 60\sigma$ and different radii, $R = 4\sigma$, 7σ, and 10σ, were modeled by one layer of wall atoms, respectively. The distance between two neighbor wall beads was 1.08σ, and the interaction parameters of LJ potential between all wall beads were set to $\varepsilon_{LJ} = 1.0k_BT$ and $\sigma = 0.8$. Wall atoms vibrate around their lattice position under a moderate harmonic potential of $\frac{1}{2}Kr^2$, where K is a spring constant that we set to 300 k_BT/σ^2, and r is the displacement of the atom from its current position to its lattice position. These choices are sufficient to prevent polymer chains from penetrating the wall.[22] The degree of confinement of both the arms

TABLE I. Molecular characteristics of star polymer melts used in the simulation.

Star polymers	f	N_{arm}	M[a]	$R_g^{(arm)}$[b]	$R_g^{(star)}$[c]
SP10 × 2	2	10	21	1.451	2.203
SP10 × 4	4	10	41	1.459	2.577
SP10 × 6	6	10	61	1.463	2.757
SP10 × 12	12	10	121	1.482	3.085
SP50 × 2	2	50	101	3.370	4.529
SP50 × 4	4	50	201	3.436	5.360
SP50 × 6	6	50	301	3.465	5.530
SP50 × 12	12	50	601	3.656	6.266
SP100 × 2	2	100	201	4.459	5.793
SP100 × 4	4	100	401	4.483	6.657
SP100 × 6	6	100	601	4.614	7.342
SP100 × 12	12	100	1201	4.801	7.751

[a]Molecular weight of a star molecule, equals to the sum of that of each arm and one core atom as $M = M_0(fN_{arm} + 1)$, where $M_0 = 1$ is the weight of one monomer.
[b]Radius of gyration R_g of each arm in the bulk (unit: σ).
[c]Radius of gyration R_g of a whole star molecule in the bulk (unit: σ).

and the entire star molecules in the different capillaries is presented in Table S I.

A $40\sigma \times 40\sigma$ square reservoir of star polymer melts with periodic boundaries perpendicular to the tube axis resides under the capillary. The interaction parameter between polymer chains and wall atoms was set to $\varepsilon_{LJ} = 1.6k_BT$ and $\sigma = 1.0$. Initially, the reservoir was sealed to prevent polymers from moving into the capillary. Following equilibration of the polymer melt, the beads in the central region connecting the capillary to the reservoir are removed, and the imbibition process begins. The height of the polymer during imbibition is determined by fitting the density profile to the following function:

$$\rho(h) = \frac{\rho_p + \rho_v}{2} - \frac{\rho_p + \rho_v}{2}\tanh\left[\frac{2(h - h_0)}{l}\right], \tag{4}$$

where ρ_p is the density of polymer melt in the capillary, $\rho_v \approx 0$ is the vapor density in the capillary due to the low polymer vapor pressure, h_0 represents the height of the interface between polymer melt and its vapor, and l stands for the thickness of the interface. The relationship between the height h and time t of the imbibition process was then monitored. The calculation methods for contrasting with the theoretical relation $h(t)$ of the Lucas–Washburn equation and evaluating the dynamics of arms or of the whole star are as follows. More calculation details have been given elsewhere.[21]

A. Surface tension

We employed Irving–Kirkwood's expression[37] to calculate the surface tension of the polymer melt. All data were derived from a flat gas–liquid interface by integrating the asymmetric part of the pressure tensor,

$$\gamma = \int_{-\lambda}^{\lambda} [P_N(z) - P_T(z)]dz. \tag{5}$$

Here, 2λ is the thickness of the whole gas–liquid interface determined by the variation of $P_N(z) - P_T(z)$, $P_N(z)$ is the normal component, and $P_T(z)$ is the tangential component to the interface of the pressure tensor. This integral should be zero both in the gas phase and in the bulk.

B. Viscosity

The viscosity of the polymer melt was calculated by creating a Poiseuille flow.[38] It was obtained by setting up two plates parallel to the xy-plate. Subsequently, the polymer melt was filled between the plates. The density of the filled melt was evaluated from the density profile of the reservoir before imbibition. Then, a body force along the x-axis was applied to every bead. Following the steady state, we fit

$$v_x(z) = \frac{\rho g_x}{2\eta}\left(C + Dz - z^2\right), \tag{6}$$

to the velocity profile along the z-axis, where v_x is the velocity being parallel to the force, ρ is the density, g_x is the body force acting on the polymer, η is the viscosity of the polymer melt, C is a constant (that equals zero when there is no-slip boundary condition), and D is the distance between two plates. Different values of g_x in the range from $0.2\ k_BT/\sigma$ to $0.6\ k_BT/\sigma$ were employed to validate the result.

C. Contact angle

The contact angle of the star polymer melt on the capillary wall was calculated by placing the same polymer droplet on a plate that has the same lattice structure and interaction parameters with the capillary. After the wetting process reached equilibrium, we fitted the shape of the droplet, and a series of contact angles were obtained.

D. Entanglements

The average number of entanglement points per arm, Z, in the system of $N_{arm} = 100$ was calculated by the primitive path analysis algorithm proposed by Everaers *et al.*[39,40] To begin with, the end atom of each arm and the core atom are fixed in space. Next, the intrachain excluded volume interactions are canceled while retaining the interchain excluded-volume interactions. Finally, the system was slowly brought to $T = 0$ to minimize its energy. The topology files used in the calculation are saved during capillary filling, and the snapshots after the operation are shown in Fig. S3. The entanglement length, N_e, is then calculated by employing

$$N_e = (N - 1)\left(\frac{\langle L_{pp}^2\rangle}{\langle R_{pp}^2\rangle} - 1\right)^{-1}, \tag{7}$$

where L_{pp} is the contour length and R_{pp} is the mean-square end-to-end distance. The number of entanglement points Z is then calculated as $Z = N/N_e$.

E. Radius of gyration

The average radius of gyration R_g of an arm or a star molecule was calculated by

$$R_g^2 = \frac{1}{n}\sum_{i=1}^{n}\left[(x_i - x_{cm})^2 + (y_i - y_{cm})^2 + (z_i - z_{cm})^2\right], \tag{8}$$

where n is the number of segments of an arm or a star molecule, the subscript i stands for the ith bead, and cm stands for the center of

mass of chains. Components of R_g are also collected by separating the tensor of R_g during imbibition,

$$R_{gz}^2 = \frac{1}{n}\sum_{i=1}^{n}(z_i - z_{cm})^2, \quad R_{gr}^2 = \frac{1}{n}\sum_{i=1}^{n}\frac{1}{2}[(x_i - x_{cm})^2 + (y_i - y_{cm})^2], \tag{9}$$

where R_{gz} is the component of R_g along the direction of capillary filling and R_{gr} is that in the radial direction.

F. Configurations

Polymer chains adsorbed to one interface have three kinds of configurations: loop, train, and tail. We defined the region within 1σ of the capillary wall as the adsorption layer. Chains with no segments in this region are viewed as free chains. The density of each state in the capillary can be calculated by $n_{conf}M_0/V_{capillary}$, where n_{conf} is the sum of the number of segments in one certain configuration and $V_{capillary}$ is the volume of the capillary. The data were collected when the wetting height was twice that of the R_g of arms, as $h > 10\sigma$.

G. Self-correlation function of the core-to-end vector

After full imbibition, the self-correlation function of the core-to-end vector of the arms was calculated by

$$C_n(t) = \frac{1}{n}\sum_{j=1}^{n}\frac{\langle \boldsymbol{r}_j(t)\cdot\boldsymbol{r}_j(0)\rangle}{\langle|\boldsymbol{r}_j(0)|^2\rangle}, \tag{10}$$

where n is the total number of arms in the capillary, and the vector $\boldsymbol{r}_j$ denotes the difference between the position of the end atom and the core atom of the jth arm.

H. Mean square displacement of core segments

The mean square displacement of core segments under confinement was calculated by

$$\begin{aligned} MSD_z(t) &= \frac{1}{n}\sum_{i=1}^{n}(z_{it} - z_{i0})^2 \\ MSD_r(t) &= \frac{1}{n}\sum_{i=1}^{n}\frac{1}{2}[(x_{it} - x_{i0})^2 + (y_{it} - y_{i0})^2], \end{aligned} \tag{11}$$

where MSD_z is the displacement along the axis of capillary, MSD_r is the displacement in the radial direction, n is the total number of core atoms in the capillary, the subscript $i0$ stands for the position of ith core atom at the initial time, and it stands for the position of ith core atom at time t.

All simulations were performed using LAMMPS[41] and carried out under a constant temperature maintained by a DPD thermostat[42] with a friction parameter $\xi = 0.5\sqrt{mk_BT/\sigma^2}$ and an interaction cutoff $r_{cut} = 2.5\sigma$. The friction parameter ξ determines the strength of the dissipative force and reflects the efficiency of keeping the temperature constant following a thermal disturbance. We used the velocity-Verlet algorithm[43] with a time step $\Delta t = 0.005\ \tau_{LJ}$ for integration, where $\tau_{LJ} = \sqrt{m\sigma^2/\varepsilon_{LJ}}$ is the standard LJ-time.

III. RESULTS AND DISCUSSION

A. Deviated imbibition dynamics from prediction of Lucas–Washburn equation

To calculate the theoretical value of the LWE prefactor, the data of surface tension γ, viscosity η, and contact angle θ for the star polymer melts were collected and plotted in Fig. 1. For linear chains, the variation of surface tension with molecular weight follows the relation $\gamma = \gamma_\infty - kM^{-1}$, where γ_∞ is the surface tension at infinite molecular weight and k is a constant determined by the nature of the polymer.[44–46] Figure 1(b) shows that the surface tension of star polymers exhibits a linear dependence on M^{-1} with functionality-dependent slopes, while the slope k increases with functionality. This further justifies the notion that, despite the very different chain topology, the major factor governing the surface tension is the presence of chain ends.[33] The variation of surface tension with N_{arm} is shown in Fig. 1(a), where the solid lines represent the fitting results using $\gamma = \gamma_\infty - KN_{arm}^{-1}$. The good fit also reveals that there should be a relation $KN_{arm}^{-1} = kM^{-1}$. Since $M \approx fN_{arm}$, we can get $K = k/f$.

Figure 1(c) shows the increasing intrinsic viscosity η of star polymers with N_{arm} or with f when N_{arm} is kept constant. Figure 1(d) shows that η decreases with f when M is kept constant, which means N_{arm} is reduced. Both results confirm that the change in arm length determines the viscosity of star polymers.[34] Due to the computational limitation, the longest arm in our simulation has a moderate level of entanglements;[21] the scaling relation follows $\eta \propto N_{arm}$ and $\eta \propto M$ (instead of exponential).

Figure 1(e) illustrates that when the solid–liquid interaction keeps constant, the contact angle θ of star polymer melts increases with N_{arm} when f is kept constant. θ also increases with f for any given N_{arm}, which might be attributed to the increasing stiffness of chains.[27,47] Figure 1(f) shows that θ increases with M, and the variation seems functionality-independent since the fitting results can overlap roughly within the margin of error. This further suggests that when discussing θ of star polymers, the parameters f and N_{arm} should be combined into M.

The theoretically predicted relations of $h(t)$ in different systems were calculated according to the data in Fig. 1 and shown as the dashed lines in Fig. 2. The actual data points for $h(t)$ according to Eq. (4) are also plotted and further fitted by solid lines. The results show that both the actual and theoretical wetting speed decrease with functionality f when N_{arm} is fixed. This can be attributed to the increase in intrinsic viscosity η with f. More significantly, with the star architecture ($f > 2$), a non-monotonic deviation of the imbibition dynamics from the theoretical LWE is observed, as with the linear chains ($f = 2$).[21] When the length of the arm is short (e.g., $N_{arm} = 10$), the imbibition process is slower than theoretically predicted. When the arm length is longer (e.g., $N_{arm} = 100$), the dynamics reverses and the filling process is faster than theoretically predicted. In previous work, a theoretical model has been established to explain the breakdown of LWE for linear polymer systems.[18] A dead zone of adsorbed polymers (i.e., reduced effective pore radius) combined with decreased free energy of the polymer under confinement slows down the imbibition process. For long-chain systems, reptation-like plug flow leads to enhanced microscopic flow of entangled chains and faster imbibition.[20,21] For star polymers, because the arms can be viewed as linear chains whose one end is spatially restricted at the star center, the mechanism behind the

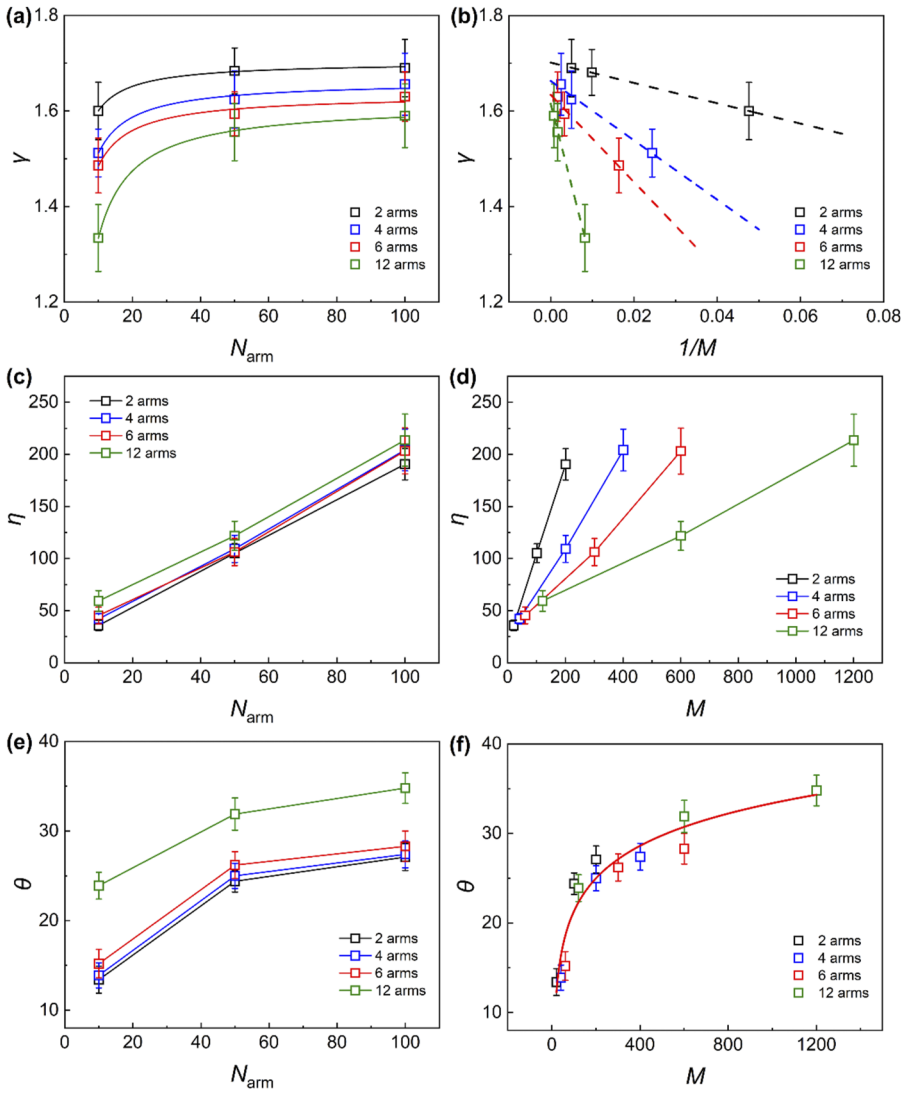

FIG. 1. Basic properties of different star polymer melts (f = 2, 4, 6, and 12) required by LWE. (a) Surface tension γ as a function of the arm length, N_{arm}, and (b) of the molecular weight M. (c) Viscosity η in the bulk as a function of the length of arm N_{arm} and (d) of the molecular weight M. (e) Contact angle θ on a plate that has the same characteristics as the capillary, as a function of the length of the arm N_{arm} and (f) of the molecular weight M.

reversal of imbibition dynamics bears similarities with that of linear polymers (i.e., the "dead zone" effect, the reptation effect, etc.). The functionality-dependent spatial restriction effect can modulate some dynamic features, such as adsorption and entanglements. This thereby influences the acceleration or deceleration effects of filling, which we will discuss in Secs. III B and III C.

Considering the critical influence of dynamic contact angle θ_d on a simple liquid,[48,49] we also calculated θ_d as a function of wetting height h, as shown in Fig. S1. The results indicate that at the beginning of imbibition ($h < 10$), θ_d decreases rapidly to a constant value slightly higher than the static contact angle θ. The difference between stable θ_d and θ increases as the arm length N_{arm} of the system decreases but does not exceed 20° at most. We further verify the effect of θ_d by comparing the actual imbibition dynamics with the prediction of the LW equation modified by θ_d, as shown in Fig. S2. The results show that the actual imbibition still deviates significantly from the theoretical prediction, which illustrates that the use of θ_d for modifying the LW equation has a very limited effect on polymer systems.

To make the trend clearer, we plot the ratios of actual prefactors A_a and theoretical prefactors A_t at different molecular weights M of the star polymer in Fig. 3. Interestingly, when M is kept constant, reducing the functionality f helps trigger the reversal. This finding suggests that it is highly beneficial to design star polymer nano-fillers with fewer arms when they need to fill pores in a short amount of time. For example, this reduced-arms strategy may help the grouting

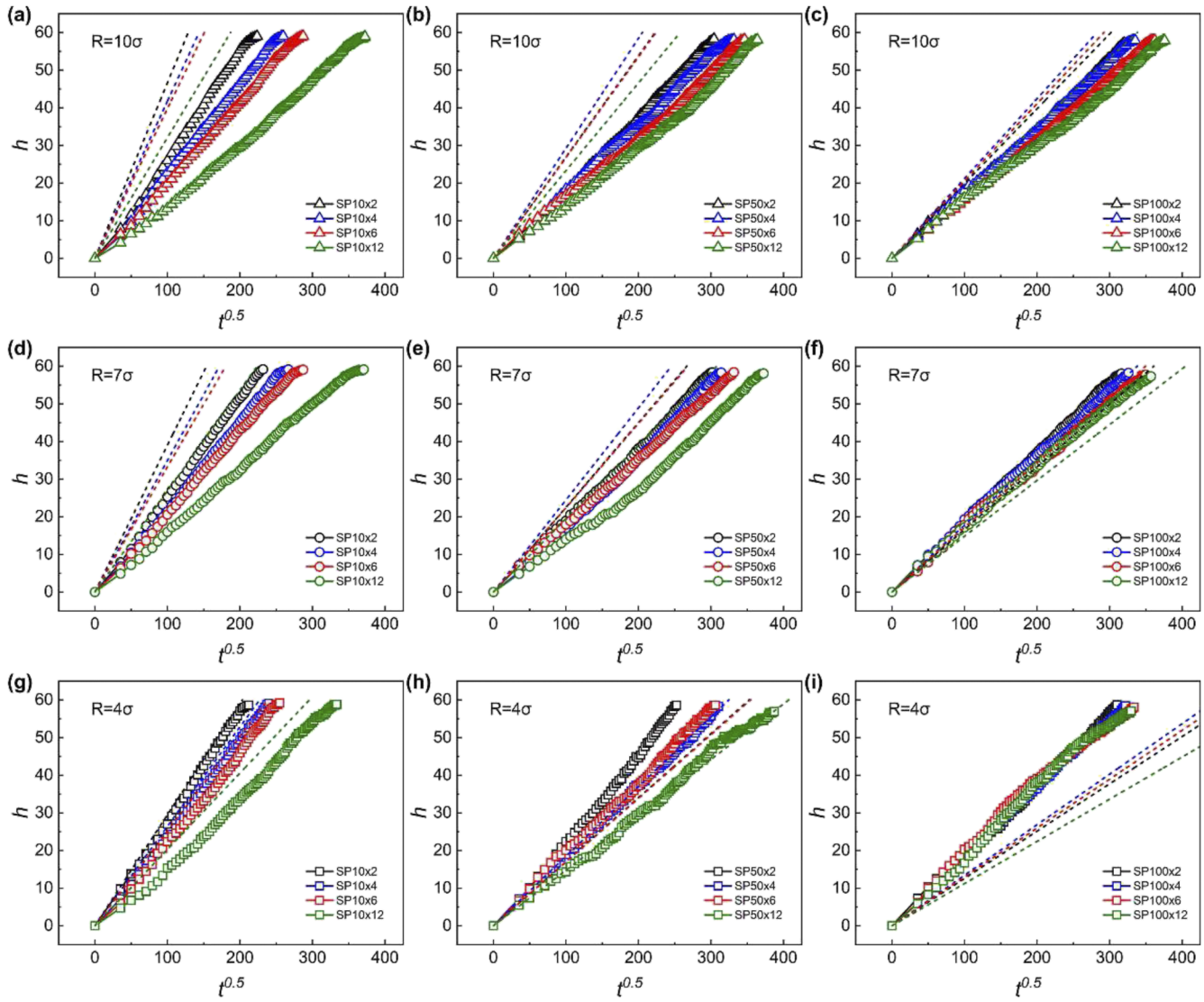

FIG. 2. Comparison of actual capillary filling with the theoretical LWE predictions for star polymer melts in nanopores with different radii, (a)–(c) $R = 10\sigma$, (d)–(f) $R = 7\sigma$, and (g)–(i) $R = 4\sigma$. The dashed lines represent the theoretical prediction of LWE, and the solid lines stand for the real imbibition processes as obtained in the simulation. Star polymer melts of different functionalities, $f = 2$, 4, 6, and 12, are represented by black lines, blue lines, red lines, and green lines, respectively.

coating of star polymers penetrate deeper into thin holes that need to be repaired, bypassing the complete curing of the coating. Additionally, Fig. 3 shows that the reversal of imbibition dynamics is strongly depending on the degree of confinement (being faster for highly confined polymers), similar to linear polymers. This further verifies the same physics behind the reversal in imbibition kinetics despite the different chain topology.

In order to show the acceleration and deceleration effects of imbibition kinetics in a comprehensive way, we calculated the effective viscosity η_{eff} of star polymer melts from the LWE as $\eta_{eff} = \gamma R \cos\theta / 2A_a^2$, as shown in Fig. 4. The relation between η_{eff} and M follows the form $\eta_{eff} \propto M^{\alpha}$, where α has been shown to depend on the degree of entanglement and confinement in linear polymers.[21] By taking the logarithm and further applying a linear fit, we obtained the value of α, which is reflected as the slope of the fitting line in Fig. 4. The result illustrates that the polymer architecture is also an important factor influencing the value of α. For symmetric star polymers, α was found to decrease with functionality. Furthermore, the effect of the star topology is more pronounced than the change in the degree of confinement in our model, as shown in Fig. 4. Therefore, we take the average α in capillaries of three radii, where $\alpha = 0.39$, 0.33, 0.28, and 0.12 for $f = 2$, 4, 6, and 12, respectively. It shows a good linear relation between α and f. In addition, from Fig. 4, the lower α in the system of higher functionality f is mainly caused by

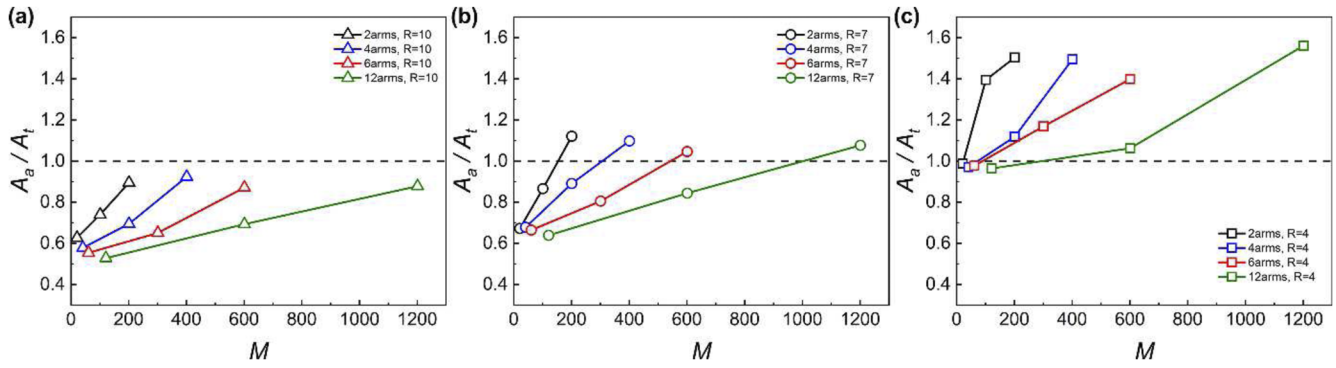

FIG. 3. Variation of the ratio of actual prefactor A_a and theoretical prefactor A_t with the molecular weight M of star polymers of different functionality (f = 2, 4, 6, and 12), in capillaries with different radii (a) $R = 4\sigma$, (b) $R = 7\sigma$, and (c) $R = 10\sigma$.

the higher η_{eff} at low M or N_{arm}. We deem that it is the stronger adsorption of high functionality star polymers that enhances the effect of the "dead zone," as recently found experimentally.[50]

B. Chain dynamics during imbibition

Understanding the behavior of chains during imbibition into a nanopore not only helps identify the physics behind the breakdown of LWE but also has practical implications for various processing techniques. According to previous works, disentanglement is the main factor that causes the low effective viscosity during capillary filling and the reversal of the imbibition dynamics.[20,21] Therefore, we first present the average number of entanglement points per arm Z at different wetting heights, h, during imbibition for the stars with N_{arm} = 100 [obtained from Eq. (7)] in Fig. 5. In this case, entanglements could be formed by two arms from different star polymers, as well as within the same star. The value of Z at $h = 0$ represents the bulk case before the onset of capillary filling. In the bulk, the higher functionality induces a higher degree of entanglement for the arms. This is mainly because, when focusing on the dynamics of arms, each arm can be considered as a linear chain with added spatial constraint at one end. Evidently, topological constraints are intensified by increasing functionality.[51,52] In the process of capillary filling, chains can only move along the "reptation tube" and are oriented due to the confinement and flow. This motional mode obviously results in reduced entanglements, which is more significant under higher degrees of confinement, as shown in Fig. 5. Furthermore, the number of remained entanglement points shows a dependence on functionality f. The system of higher f is prone to retain more entanglement points. However, this effect gradually weakens with an increasing degree of confinement. In the case of $R = 4\sigma$, where the degree of confinement on the arms of N_{arm} = 100 is greater than 1 (i.e., $R_g^{(arm)} > R$), the number of remained entanglement points of each system is roughly equal.

Of particular importance is understanding the distribution of remained entanglement points within the capillary, as it provides insights into the varying strength of topological constraints at different positions. The primitive path analysis algorithm proposed by Everaers *et al.*[39,40] is no doubt a strong tool to obtain the number of entanglement points, but it does not suffice for calculating their exact locations. Therefore, we can only approximately judge the location of the original entanglement points by the topological snapshots, as

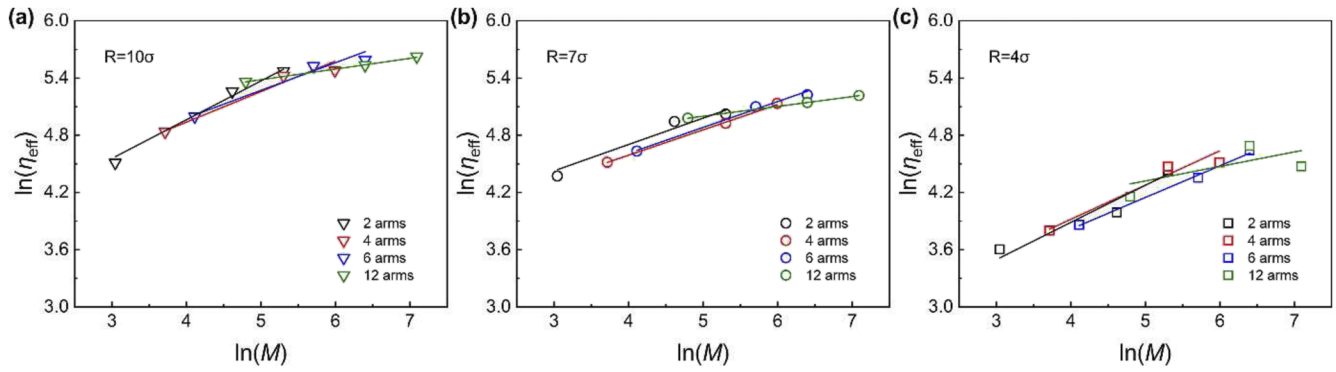

FIG. 4. Variation of the effective viscosity η_{eff} with the molecular weight M of star polymers of different functionality (f = 2, 4, 6, and 12) in capillaries with different radii (a) $R = 4\sigma$, (b) $R = 7\sigma$, and (c) $R = 10\sigma$.

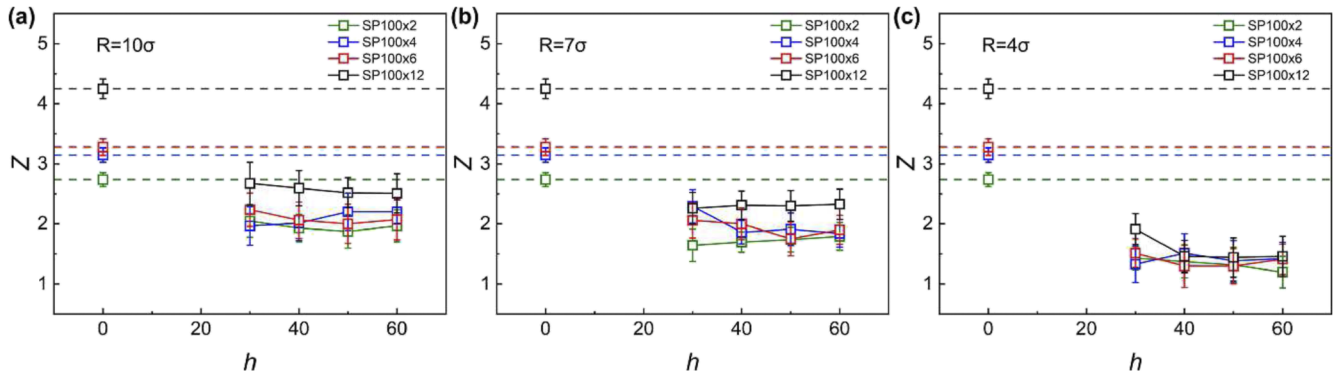

FIG. 5. Variation of the average number of entanglement points per arm Z of star polymers of N_{arm} = 100 with the wetting height h during imbibition in the cases of (a) $R = 10\sigma$, (b) $R = 7\sigma$, and (c) $R = 4\sigma$.

shown in Fig. S3. The snapshots show that the remained entanglement points are mainly distributed in the vicinity of the capillary wall and the front of the flow. The former one is caused by extra topological constraints imposed by the adsorbed arms as observed experimentally,[50] and the latter one is induced by the radial velocity component at the front of the flow.[22]

The orientational stretching due to the special motional mode under confinement is considered the reason for the disentanglement of chains.[20,21] Therefore, we utilized Eq. (8) to calculate the average radius of gyration R_g of the arms within the nanopores during imbibition, and the result is shown in Fig. 6. The initial value of R_g at $h = 0$ stands for the R_g of arms in the bulk (before the imbibition). In Fig. 6, a clear extension of arms can be observed during capillary filling under confinement for systems with N_{arm} = 50 and 100. For systems with N_{arm} = 10, these short arms make it difficult to form random coils initially (i.e., short arms are already stretched), so the change in R_g is very slight. As the capillary is close to being completely filled, the effect of flow gradually diminishes, and this extension exhibits a tendency to revert back. Both the length of the arms and the degree of confinement contribute to an increase in the maximum extension and recovery time. Hence, it can be concluded that flow initiates the extension of chains, while the degree of confinement determines the extent of extension, which subsequently influences the degree of disentanglement. However, it is difficult to identify a clear functionality dependence of the degree of extension for star polymers. The R_g (h) curves of stars bearing the same N_{arm} but different f nearly overlap. It suggests that though the spatial restriction imposed on the ends of arms is strengthened as f increases, its impact on the extension of arms during the imbibition process is weak.

Besides the average radius of gyration R_g of the arms, we also calculated the R_g of the whole stars within the nanopores. In order to demonstrate the change in the shape of the stars during imbibition, we separated the components of R_g along the direction of the capillary filling (R_{gz}) and in the radial direction (R_{gr}) by Eq. (9). The ratio of R_{gz} and R_{gr} describes the shape of star polymers. Generally, the value of R_{gz}/R_{gr} of coil-like chains in the static bulk is around 1, especially for the star polymers. Figure 7 reveals that the shape of star molecules undergoes a transformation from spherical to ellipsoidal during capillary filling as R_{gz} becomes larger than R_{gr}. Furthermore, the degree of shape change depends on functionality f. Star polymers with a larger number of arms are more likely to keep

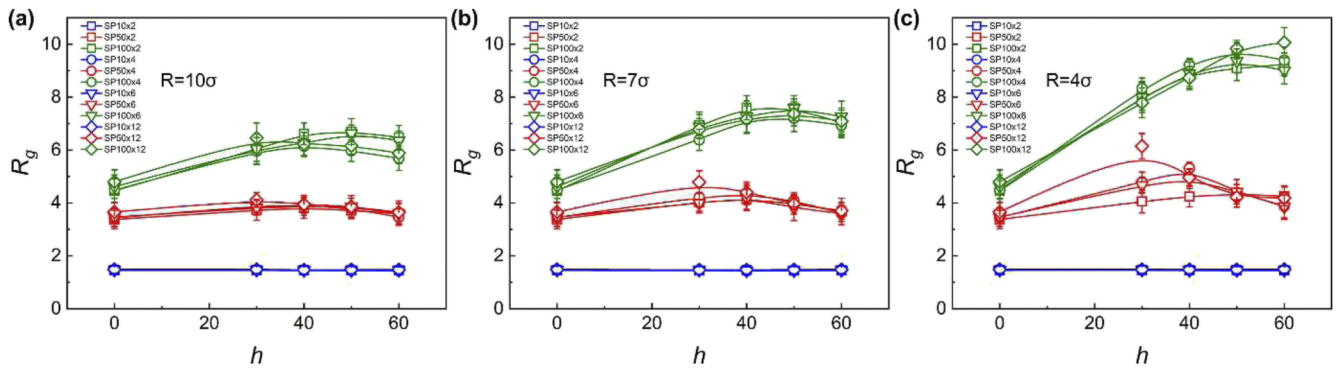

FIG. 6. Variation of the average radius of gyration R_g of the arms in the capillary with the wetting height h during the imbibition processes in the cases of (a) $R = 10\sigma$, (b) $R = 7\sigma$, and (c) $R = 4\sigma$.

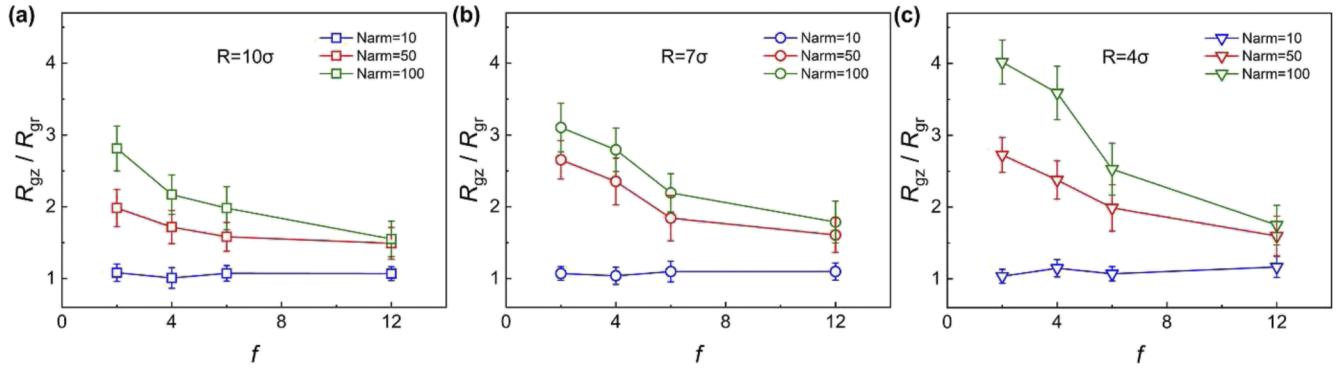

FIG. 7. The ratio of the components of R_g of the whole star polymer along the direction of capillary filling R_{gz} and in the radial direction R_{gr} within capillaries is (a) $R = 10\sigma$, (b) $R = 7\sigma$, and (c) $R = 4\sigma$. The data are collected when the wetting height is more than twice the R_g of arms in static status. The curves reflect the relation between the change in shape of star molecules and their functionality f during nanopore filling.

their original spherical shape. This can be attributed to the increased stiffness of star polymers with high functionality f.[27] To further prove that, we collected the distribution of both the core atoms of star molecules and the end atoms of the arms during imbibition, as shown in Figs. S4 and S5. Figure S4 shows that the core atoms in the systems of $f \leq 4$ can still be adsorbed on the capillary wall, as they are distributed over the entire range from $r = 0$ to $r = R$. For the stars with $f = 6$ and $f = 12$, the core atoms can only be found outside a certain distance from the wall, as from $r = 0$ to $r < R$. In addition, this distance increases with functionality f. This observation suggests the presence of a rigid region near the core segments due to the star architecture, and this region expands with higher functionality f. Once f surpasses a certain threshold, the core segments are no longer able to be adsorbed on the capillary wall. Consequently, the configurational entropy contributed by the core atoms adsorbed on the wall decreases. Figure S5 shows that the end atoms of all systems have a uniform distribution over the entire range from $r = 0$ to $r = R$. This indicates that the adsorption of end atoms is less influenced by chain topology.

Chains near the capillary wall have to pass through several unfavorable configurations before being completely adsorbed, such as loops and trains.[23,24] This process determines the extremely long adsorption time, as experimentally found.[53] In simulation, we calculated the number of monomers in each configuration (loops, trains, tails, and free chains) during the whole imbibition process and then obtained the density of each configuration in the capillary, ρ_{loop}, ρ_{train}, ρ_{tail}, and ρ_{free}. The development of ρ_{loop}, ρ_{train}, ρ_{tail}, and ρ_{free} with the wetting time t is shown in Fig. S6. At the first stage, all the density values increase because more arms are constantly entering the capillary. After a period of wetting, the number of segments in each configuration remained constant. The density of the different configurations then forms a stable ratio. Subsequently, we extracted the final density of all systems, and the result is depicted in Fig. 8. For loops and trains, with both ends fixed on the wall, the final density is significantly higher in the systems with longer N_{arm}. The increase in the degree of confinement also increases the number of such configurations since the specific surface area for adsorption increases. In addition, ρ_{loop} and ρ_{train} slightly increase with functionality f when $N_{arm} = 10$, but they no longer depend on f when $N_{arm} = 50$ and $N_{arm} = 100$. It demonstrates that star topologies with high functionality f make arms more prone to being adsorbed and form loops or trains. However, this effect is gradually weakened with increasing N_{arm}. For tails, the configuration of adsorbed arms is such that only one end is fixed on the wall and another is free. When the capillary radius is comparable to the chain length, it is difficult for arms to form long tails under such extreme confinement. So the final density of tails ρ_{tail} decreases with the degree of confinement and is lower than ρ_{loop} and ρ_{train}. For the density of free arms, ρ_{free} indirectly reflects the amount of adsorption. Figure 8 illustrates that ρ_{free} decreases both with N_{arm} and the degree of confinement. This demonstrates that systems of higher N_{arm} can induce a thicker adsorption layer in the capillary with the same radius. Additionally, the increasing specific surface area of the wall when the capillary radius decreases also leads to a higher amount of adsorption.

C. Chain dynamics after full imbibition

Following the full imbibition of polymer chains in the capillaries, chains require a period of time to relax toward their equilibrium state under confinement. Recent experiments in type-A polymers confined in cylindrical nanopores have shown very long equilibration times that depend on temperature, pore size, and chain topology.[54] It was shown that star-shaped polymers require longer times to reach equilibrium as compared to linear polymers because of their higher tendency for adsorption.

Therefore, discussing the chain dynamics following imbibition is also relevant in simulations. In order to evaluate the arm relaxation, we calculated the average self-correlation function of the core-to-end vector, as shown in Fig. 9. The data were collected immediately after the complete imbibition of the star polymers. Therefore, it well reflects the ability of chains to revert back to their equilibrium state after being disturbed under extreme confinement. The result in Fig. 9 shows that the self-correlation function in the systems of higher N_{arm} decays at a much slower rate, which means long arms require extremely long times to reach equilibrium. This time exceeds the entire wetting time needed to fill the nanopores.

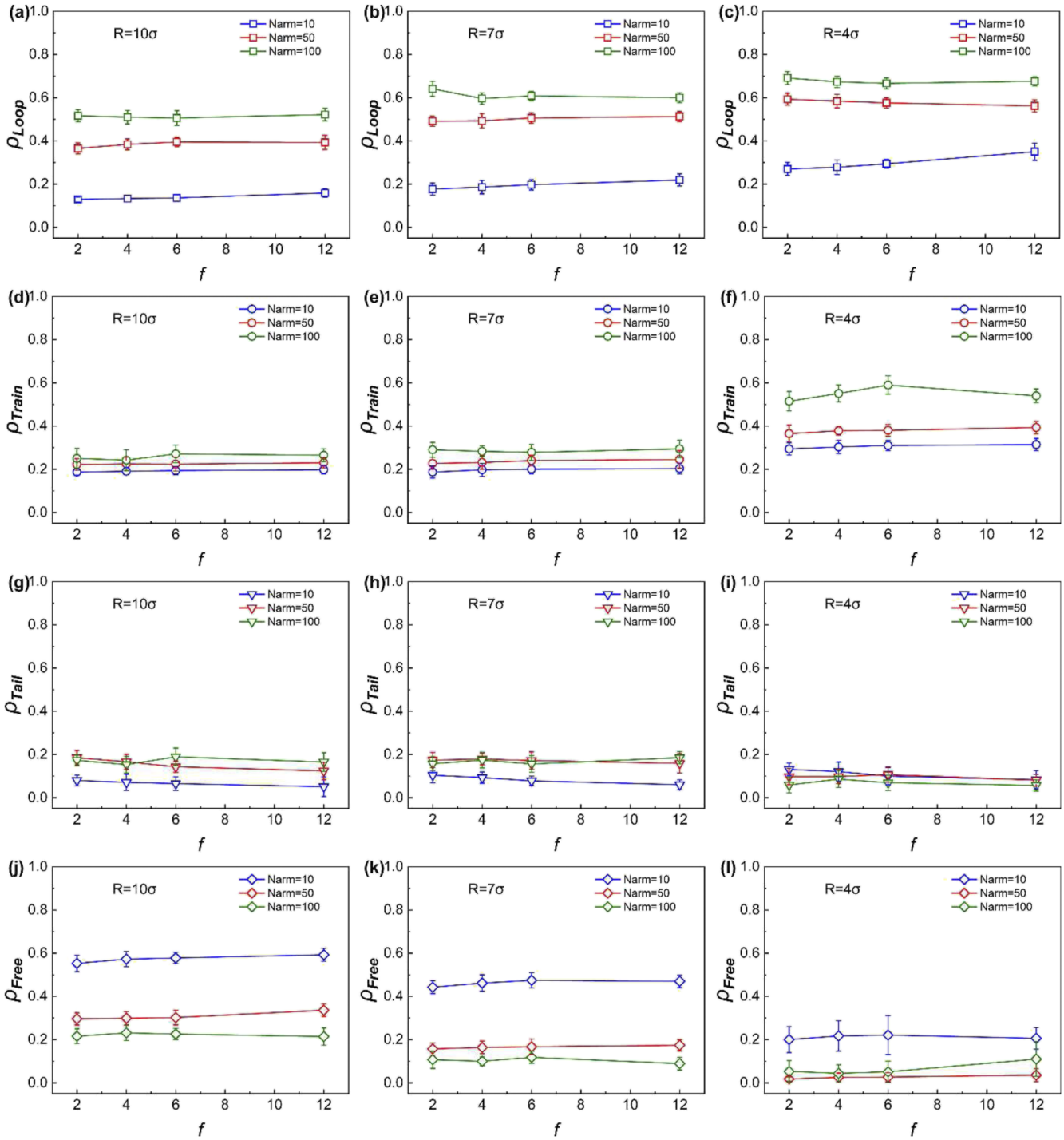

FIG. 8. The final density of adsorbed arms in three types of configurations (a)–(c) the density of loop ρ_{loop}, (d)–(f) the density of train ρ_{train}, (g)–(i) the density of tail ρ_{tail}, and density of free chains ρ_{free}, (j)–(l) in the capillaries with different radii ($R = 10\sigma$, $R = 7\sigma$, and $R = 4$).

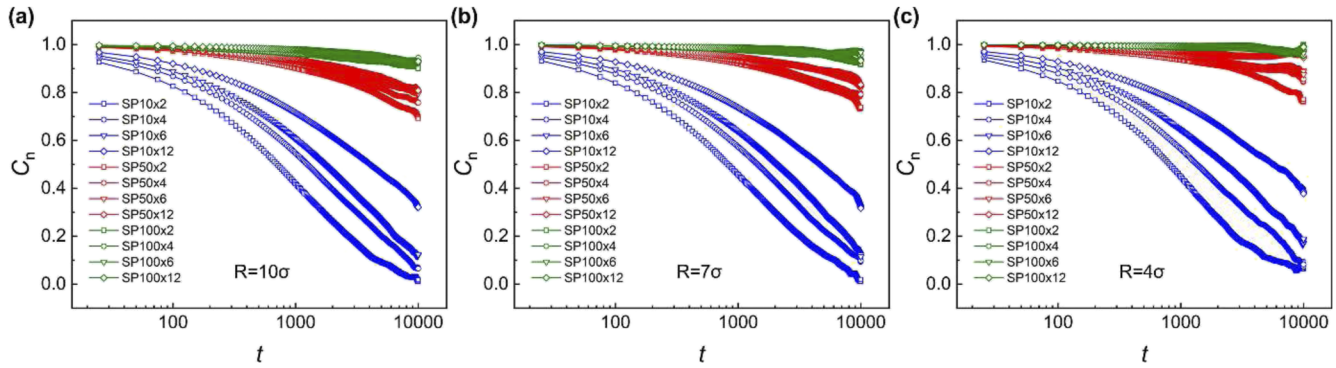

FIG. 9. Variation of the self-correlation function of the core-to-end vector of the arms C_n in the capillaries of (a) $R = 10\sigma$, (b) $R = 7\sigma$, and (c) $R = 4\sigma$, during 10 000 time units after full imbibition. Lines in different colors represent the systems of $N_{arm} = 10$ (blue), $N_{arm} = 50$ (red), and $N_{arm} = 100$ (green), respectively. Lines with different shapes of points represent the systems of $f = 2$ (square), $f = 4$ (circle), $f = 6$ (triangle), and $f = 12$ (rhombus), respectively.

Moreover, the self-correlation function also decays more slowly in the system of higher functionality f when the N_{arm} of the system is kept constant. This is because star polymers rely on the cooperative relaxation of multiple arms to reach an equilibrium state. The higher the functionality f of the star polymers, the longer the process is due to the broadening of the distribution of the relaxation times observed through dielectric spectroscopy.[50] In addition to functionality, the degree of confinement exerts a strong influence on arm relaxation. To show this, we plot in Fig. S7 the data as a function of capillary radii. The result illustrates that stars with the same N_{arm} and f require a longer relaxation time to reach equilibrium under a higher degree of confinement.

As the diffusion of molecules is also sensitive to macromolecular topology, we have evaluated the dynamics from the mean-square

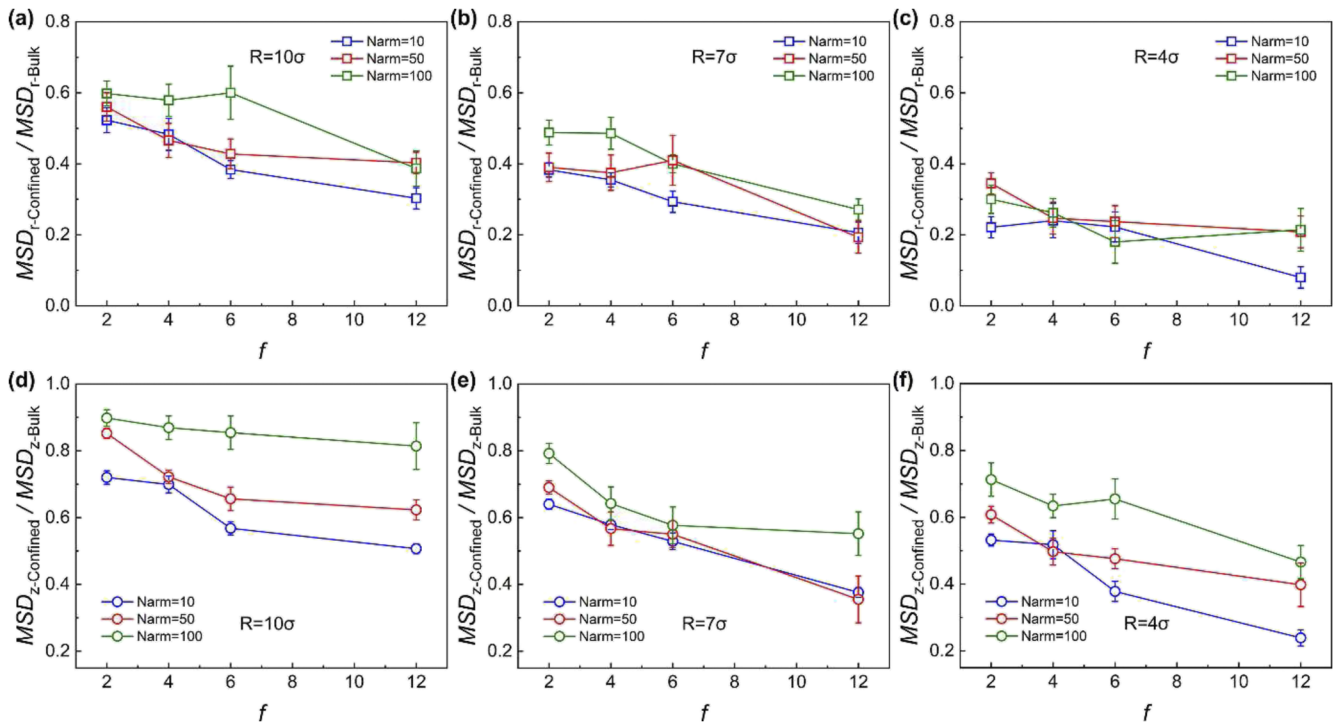

FIG. 10. The ratio of the mean square displacement of core segments under confinement and in the bulk, in the cases of (a)–(c) in the radial direction, $MSD_{r-Confined}/MSD_{r-Bulk}$ and (d)–(f) along the axis of capillary, $MSD_{z-Confined}/MSD_{z-Bulk}$, in the capillaries of $R = 10\sigma$, $R = 7\sigma$, and $R = 4\sigma$, respectively.

displacement, *MSD*, of core segments for each star polymer. The evolution of *MSD* for the core segments in the bulk is depicted in Fig. S8. The result shows that the *MSD* of core segments decreases both with increasing functionality f and N_{arm}. This reflects the increasing intermolecular friction of star polymers with increasing f or N_{arm}, which further determines the intrinsic viscosity. We also calculated (Fig. S8) the development of *MSD* of core segments in the capillary after arms relax for 20 000 time steps following the full imbibition. Because of confinement, interfacial friction, and adsorption, both $MSD_{r-Confined}$ and $MSD_{z-Confined}$ decrease below the corresponding bulk value. Interestingly, the degree of reduction is approximately constant, i.e., independent of time. The result is plotted in Fig. 10 as a function of star functionality and N_{arm}. It depicts decreasing $MSD_{r-Confined}/MSD_{r-Bulk}$ and $MSD_{z-Confined}/MSD_{z-Bulk}$ for the shorter arms. This reflects an increasing fraction of adsorbed sites with decreasing N_{arm} and the concomitant enhancement of the adsorption of core segments. $MSD_{r-Confined}/MSD_{r-Bulk}$ and $MSD_{z-Confined}/MSD_{z-Bulk}$ also decrease with increasing functionality. It further illustrates that star polymers with a higher number of arms undergo a stronger effect of adsorption and friction, in agreement with recent experiments.[53] Additionally, the increase in the degree of confinement results in lower $MSD_{r-Confined}/MSD_{r-Bulk}$ and $MSD_{z-Confined}/MSD_{z-Bulk}$, with the effect being more pronounced in the former.

IV. CONCLUSIONS

In conclusion, the imbibition process of star polymer melts exhibits a reversal in the dynamics of imbibition in nanopores. Systems of shorter arm length N_{arm} penetrate slower than predicted by the LWE, while systems with longer arm length N_{arm} penetrate faster. The physics behind the phenomenon should be the same as for linear-chain polymers, reflecting the balance between the effects of "dead zone" and disentanglement. A useful strategy to trigger the faster-than-prediction capillary filling of star polymer melts is to decrease their functionality f under a constant molecular weight.

The arms of star polymers with higher f exhibit a higher degree of entanglement in the bulk. Under flow, the arms are stretched, causing chains to disentangle. This effect is enhanced with an increasing degree of confinement. The remaining entanglements are mainly distributed in the vicinity of the capillary wall and at the front of the flow. The star topology induces a stiff region near the core segment, which increases with f. In addition, systems of higher f experience stronger adsorption and are more prone to form the configuration of loops and trains. However, this effect is gradually weakened with increasing N_{arm}.

After full imbibition, the arms of star polymers take a longer time than linear chains to reach the equilibrium state, in excellent agreement with recent experiments. Moreover, this time increases with functionality f, N_{arm}, and degree of confinement. Additionally, the reduced normalized mean square of displacement of core segments following capillary filling reveals stronger adsorption and friction in the systems of higher f.

SUPPLEMENTARY MATERIAL

See the supplementary material for the degree of confinement, dynamic contact angle, snapshots of entanglement, distribution of core atoms and end atoms, configurations in the capillary, self-correlation function of the core-to-end vector of arms, and mean square of displacement of core segments.

ACKNOWLEDGMENTS

This research was supported the National Key R & D Program of China (Grant No. 2022YFE0103800), the National Natural Science Foundation of China (Grant No. 21774004), the Recruitment Program of Guangdong (Grant No. 2016ZT06C322), and the 111 Project (No. B18023). Jianwei Zhang acknowledges the funding supported by the China Scholarship Council. The computation of this work was made possible by the facilities of Information and Network Engineering and Research Center of SCUT.

AUTHOR DECLARATIONS

Conflict of Interest

The authors have no conflicts to disclose.

Author Contributions

Jianwei Zhang: Conceptualization (equal); Investigation (equal); Writing – original draft (equal); Writing – review & editing (equal). **Jinyu Lei**: Resources (equal). **Pu Feng**: Resources (equal). **George Floudas**: Investigation (equal); Writing – review & editing (equal). **Guangzhao Zhang**: Supervision (equal); Writing – review & editing (equal). **Jiajia Zhou**: Conceptualization (equal); Investigation (equal); Supervision (equal); Writing – review & editing (equal).

DATA AVAILABILITY

The data that support the findings of this study are available from the corresponding authors upon reasonable request.

REFERENCES

[1]G. Lapienis, "Star-shaped polymers having PEO arms," Prog. Polym. Sci. **34**, 852–892 (2009).
[2]J. M. Ren, T. G. McKenzie, Q. Fu, E. H. H. Wong, J. Xu, Z. An, S. Shanmugam, T. P. Davis, C. Boyer, and G. G. Qiao, "Star polymers," Chem. Rev. **116**, 6743–6836 (2016).
[3]J. D. Beard, D. Rouholamin, B. L. Farmer, K. E. Evans, and O. R. Ghita, "Control and modelling of capillary flow of epoxy resin in aligned carbon nanotube forests," RSC Adv. **5**, 39433–39441 (2015).
[4]K. Shin, S. Obukhov, J.-T. Chen, J. Huh, Y. Hwang, S. Mok, P. Dobriyal, P. Thiyagarajan, and T. P. Russell, "Enhanced mobility of confined polymers," Nat. Mater. **6**, 961–965 (2007).
[5]B. Kwon, J. Molek, and A. L. Zydney, "Ultrafiltration of PEGylated proteins: Fouling and concentration polarization effects," J. Membr. Sci. **319**, 206–213 (2008).
[6]J. C. T. Eijkel and A. van den Berg, "Nanofluidics: What is it and what can we expect from it?," Microfluid. Nanofluid. **1**, 249–267 (2005).
[7]S. Jin and G. B. McKenna, "Effect of nanoconfinement on polymer chain dynamics," Macromolecules **53**, 10212–10216 (2020).
[8]N. K. Lee, J. Farago, H. Meyer, J. P. Wittmer, J. Baschnagel, S. P. Obukhov, and A. Johner, "Non-ideality of polymer melts confined to nanotubes," Europhys. Lett. **93**, 48002 (2011).

[9]N. K. Lee, D. Diddens, H. Meyer, and A. Johner, "Local chain segregation and entanglements in a confined polymer melt," Phys. Rev. Lett. **118**, 067802 (2017).
[10]R. Lucas, "Ueber das Zeitgesetz des kapillaren Aufstiegs von Flüssigkeiten," Kolloid-Z. **23**, 15–22 (1918).
[11]E. W. Washburn, "The dynamics of capillary flow," Phys. Rev. **17**, 273 (1921).
[12]Y. Yao, S. Alexandris, F. Henrich, G. Auernhammer, M. Steinhart, H. J. Butt, and G. Floudas, "Complex dynamics of capillary imbibition of poly(ethylene oxide) melts in nanoporous alumina," J. Chem. Phys. **146**, 203320 (2017).
[13]Y. Yao, H.-J. Butt, J. Zhou, M. Doi, and G. Floudas, "Capillary imbibition of polymer mixtures in nanopores," Macromolecules **51**, 3059–3065 (2018).
[14]C.-H. Tu, M. Steinhart, H.-J. Butt, and G. Floudas, "*In situ* monitoring of the imbibition of poly(*n*-butyl methacrylates) in nanoporous alumina by dielectric spectroscopy," Macromolecules **52**, 8167–8176 (2019).
[15]R. B. Venkatesh, N. Manohar, Y. Qiang, H. Wang, H. H. Tran, B. Q. Kim, A. Neuman, T. Ren, Z. Fakhraai, R. A. Riggleman, K. J. Stebe, K. Turner, and D. Lee, "Polymer-infiltrated nanoparticle films using capillarity-based techniques: Toward multifunctional coatings and membranes," Annu. Rev. Chem. Biomol. Eng. **12**, 411–437 (2021).
[16]J. L. Hor, H. Wang, Z. Fakhraai, and D. Lee, "Effect of physical nanoconfinement on the viscosity of unentangled polymers during capillary rise infiltration," Macromolecules **51**, 5069–5078 (2018).
[17]J. L. Hor, H. Wang, Z. Fakhraai, and D. Lee, "Effects of polymer–nanoparticle interactions on the viscosity of unentangled polymers under extreme nanoconfinement during capillary rise infiltration," Soft Matter **14**, 2438–2446 (2018).
[18]Y. Yao, H. J. Butt, G. Floudas, J. Zhou, and M. Doi, "Theory on capillary filling of polymer melts in nanopores," Macromol. Rapid Commun. **39**, e1800087 (2018).
[19]R. B. Venkatesh and D. Lee, "Conflicting effects of extreme nanoconfinement on the translational and segmental motion of entangled polymers," Macromolecules **55**, 4492–4501 (2022).
[20]R. B. Venkatesh and D. Lee, "Interfacial friction controls the motion of confined polymers in the pores of nanoparticle packings," Macromolecules **55**, 8659–8667 (2022).
[21]J. Zhang, J. Lei, W. Tian, G. Zhang, G. Floudas, and J. Zhou, "Capillary filling of polymer chains in nanopores," Macromolecules **56**, 2258–2267 (2023).
[22]D. I. Dimitrov, A. Milchev, and K. Binder, "Capillary rise in nanopores: Molecular dynamics evidence for the Lucas–Washburn equation," Phys. Rev. Lett. **99**, 054501 (2007).
[23]C. H. Tu, J. Zhou, M. Doi, H. J. Butt, and G. Floudas, "Interfacial interactions during *in situ* polymer imbibition in nanopores," Phys. Rev. Lett. **125**, 127802 (2020).
[24]C.-H. Tu, J. Zhou, H.-J. Butt, and G. Floudas, "Adsorption kinetics of *cis*-1,4-polyisoprene in nanopores by *in situ* nanodielectric spectroscopy," Macromolecules **54**, 6267–6274 (2021).
[25]P. Kardasis, N. Kalafatakis, M. Gauthier, D. Vlassopoulos, and G. Floudas, "Layers of distinct mobility in densely grafted dendrimer arborescent polymer hybrids," Phys. Rev. Lett. **126**, 207802 (2021).
[26]P. Bačová, L. G. D. Hawke, D. J. Read, and A. J. Moreno, "Dynamics of branched polymers: A combined study by molecular dynamics simulations and tube theory," Macromolecules **46**, 4633–4650 (2013).
[27]J. Fan, H. Emamy, A. Chremos, J. F. Douglas, and F. W. Starr, "Dynamic heterogeneity and collective motion in star polymer melts," J. Chem. Phys. **152**, 054904 (2020).
[28]A. Chremos, P. J. Camp, E. Glynos, and V. Koutsos, "Adsorption of star polymers: Computer simulations," Soft Matter **6**, 1483–1493 (2010).
[29]H. E. Johnson, J. F. Douglas, and S. Granick, "Topological influences on polymer adsorption and desorption dynamics," Phys. Rev. Lett. **70**, 3267–3270 (1993).
[30]E. Glynos, A. Chremos, G. Petekidis, P. J. Camp, and V. Koutsos, "Polymer-like to soft colloid-like behavior of regular star polymers adsorbed on surfaces," Macromolecules **40**, 6947–6958 (2007).
[31]F. Vargas-Lara, B. A. Pazmino Betancourt, and J. F. Douglas, "Communication: A comparison between the solution properties of knotted ring and star polymers," J. Chem. Phys. **149**, 161101 (2018).
[32]Q. Zhou and R. G. Larson, "Direct molecular dynamics simulation of branch point motion in asymmetric star polymer melts," Macromolecules **40**, 3443–3449 (2007).
[33]Z. Y. Qian, V. S. Minnikanti, B. B. Sauer, G. T. Dee, and L. A. Archer, "Surface tension of symmetric star polymer melts," Macromolecules **41**, 5007–5013 (2008).
[34]B. Mendrek and B. Trzebicka, "Synthesis and characterization of well-defined poly(*tert*-butyl acrylate) star polymers," Eur. Polym. J. **45**, 1979–1993 (2009).
[35]D. Frenkel, B. Smit, and M. A. Ratner, *Understanding Molecular Simulation: From Algorithms to Applications* (Academic Press, San Diego, 1996).
[36]K. Kremer and G. S. Grest, "Dynamics of entangled linear polymer melts: A molecular-dynamics simulation," J. Chem. Phys. **92**, 5057–5086 (1990).
[37]J. Irving and J. G. Kirkwood, "The statistical mechanical theory of transport processes. IV. The equations of hydrodynamics," J. Chem. Phys. **18**, 817–829 (1950).
[38]J. A. Backer, C. P. Lowe, H. C. Hoefsloot, and P. D. Iedema, "Poiseuille flow to measure the viscosity of particle model fluids," J. Chem. Phys. **122**, 154503 (2005).
[39]R. Everaers, S. K. Sukumaran, G. S. Grest, C. Svaneborg, A. Sivasubramanian, and K. Kremer, "Rheology and microscopic topology of entangled polymeric liquids," Science **303**, 823–826 (2004).
[40]S. K. Sukumaran, G. S. Grest, K. Kremer, and R. Everaers, "Identifying the primitive path mesh in entangled polymer liquids," J. Polym. Sci., Part B: Polym. Phys. **43**, 917–933 (2005).
[41]S. Plimpton, "Fast parallel algorithms for short-range molecular dynamics," J. Comput. Phys. **117**, 1–19 (1995).
[42]T. Soddemann, B. Dünweg, and K. Kremer, "Dissipative particle dynamics: A useful thermostat for equilibrium and nonequilibrium molecular dynamics simulations," Phys. Rev. E **68**, 046702 (2003).
[43]M. P. Allen and D. J. Tildesley, *Computer Simulation of Liquids* (Oxford University Press, Oxford, UK, 2017).
[44]M. Aubouy, M. Manghi, and E. Raphael, "Interfacial properties of polymeric liquids," Phys. Rev. Lett. **84**, 4858–4861 (2000).
[45]S. K. Kumar and R. L. Jones, "Dominance of density variations in determining the molecular weight dependence of surface tensions of polymer melts," Adv. Colloid Interface Sci. **94**, 33–38 (2001).
[46]C. Meddah, A. Milchev, S. A. Sabeur, and A. M. Skvortsov, "Molecular weight effects on interfacial properties of linear and ring polymer melts: A molecular dynamics study," J. Chem. Phys. **145**, 194902 (2016).
[47]J. Midya, S. A. Egorov, K. Binder, and A. Nikoubashman, "Wetting transitions of polymer solutions: Effects of chain length and chain stiffness," J. Chem. Phys. **156**, 044901 (2022).
[48]B. Henrich, C. Cupelli, M. Santer, and M. Moseler, "Continuum concepts in nanoscale capillary impregnation," New J. Phys. **10**, 113022 (2008).
[49]C. Cupelli, B. Henrich, T. Glatzel, R. Zengerle, M. Moseler, and M. Santer, "Dynamic capillary wetting studied with dissipative particle dynamics," New J. Phys. **10**, 043009 (2008).
[50]P. Kardasis, A. Oikonomopoulos, G. Sakellariou, M. Steinhart, and G. Floudas, "Effect of star architecture on the dynamics of 1,4-*cis*-polyisoprene under nanometer confinement," Macromolecules **54**, 11392–11403 (2021).
[51]J. Cao and Z. Wang, "Microscopic picture of constraint release effects in entangled star polymer melts," Macromolecules **49**, 5677–5691 (2016).
[52]C. Schubert, C. Osterwinter, C. Tonhauser, M. Schömer, D. Wilms, H. Frey, and C. Friedrich, "Can hyperbranched polymers entangle? Effect of hydrogen bonding on entanglement transition and thermorheological properties of hyperbranched polyglycerol melts," Macromolecules **49**, 8722–8737 (2016).
[53]P. Kardasis, G. Sakellariou, and G. Floudas, "Ultraslow adsorption of star *cis*-1,4-polyisoprenes by in situ imbibition in nanopores," Macromolecules (published online, 2024).
[54]P. Kardasis, G. Sakellariou, M. Steinhart, and G. Floudas, "Non-equilibrium effects of polymer dynamics under nanometer confinement: Effects of architecture and molar mass," J. Phys. Chem. B **126**, 5570–5581 (2022).

Support Information

Capillary Filling of Star Polymer Melts in Nanopores

Jianwei Zhang[1], Jinyu Lei[1], Pu Feng[2], George Floudas[3,4,5], Guangzhao Zhang[1,*], and Jiajia Zhou[6,7,*]

1. Faculty of Materials Science and Engineering, South China University of Technology, Guangzhou 510640, China
2. School of Civil Engineering and Transportation, South China University of Technology, Guangzhou 510640, China
3. Max Planck Institute for Polymer Research, 55128 Mainz, Germany
4. Department of Physics, University of Ioannina, 45110 Ioannina, Greece
5. Institute of Materials Science and Computing, University Research Center of Ioannina (URCI), 45110 Ioannina, Greece
6. South China Advanced Institute for Soft Matter Science and Technology, School of Emergent Soft Matter, South China University of Technology, Guangzhou 510640, China
7. Guangdong Provincial Key Laboratory of Functional and Intelligent Hybrid Materials and Devices, South China University of Technology, Guangzhou 510640, China

Contents

1. Degree of confinement
2. Dynamic contact angle
3. Entanglement
4. Distribution of core atoms and end atoms
5. Configurations in the capillary
6. Self-correlation function of the core-to-end vector
7. Mean square displacement of core segments

1. Degree of confinement

TABLE S I. Degree of Confinement on Arms and Stars in Simulation.

Star polymers	$R_g^{(arm)}/R_1^{(a}$	$R_g^{(arm)}/R_2^{(b}$	$R_g^{(arm)}/R_3^{(c}$	$R_g^{(star)}/R_1$	$R_g^{(star)}/R_2$	$R_g^{(star)}/R_3$
SP10x2	0.15	0.21	0.36	0.22	0.31	0.55
SP10x4	0.15	0.21	0.36	0.26	0.37	0.64
SP10x6	0.15	0.21	0.37	0.28	0.39	0.69
SP10x12	0.15	0.21	0.37	0.31	0.44	0.77
SP50x2	0.34	0.48	0.84	0.45	0.65	1.13
SP50x4	0.34	0.49	0.86	0.54	0.77	1.34
SP50x6	0.35	0.50	0.87	0.55	0.79	1.38
SP50x12	0.37	0.52	0.91	0.63	0.90	1.57
SP100x2	0.45	0.64	1.11	0.58	0.83	1.45
SP100x4	0.45	0.64	1.12	0.67	0.95	1.66
SP100x6	0.46	0.66	1.15	0.73	1.05	1.84
SP100x12	0.48	0.69	1.20	0.78	1.11	1.94

[a)] $R_1 = 10\,\sigma$. [b)] $R_2 = 7\,\sigma$. [c)] $R_3 = 4\,\sigma$.

2. Dynamic contact angle

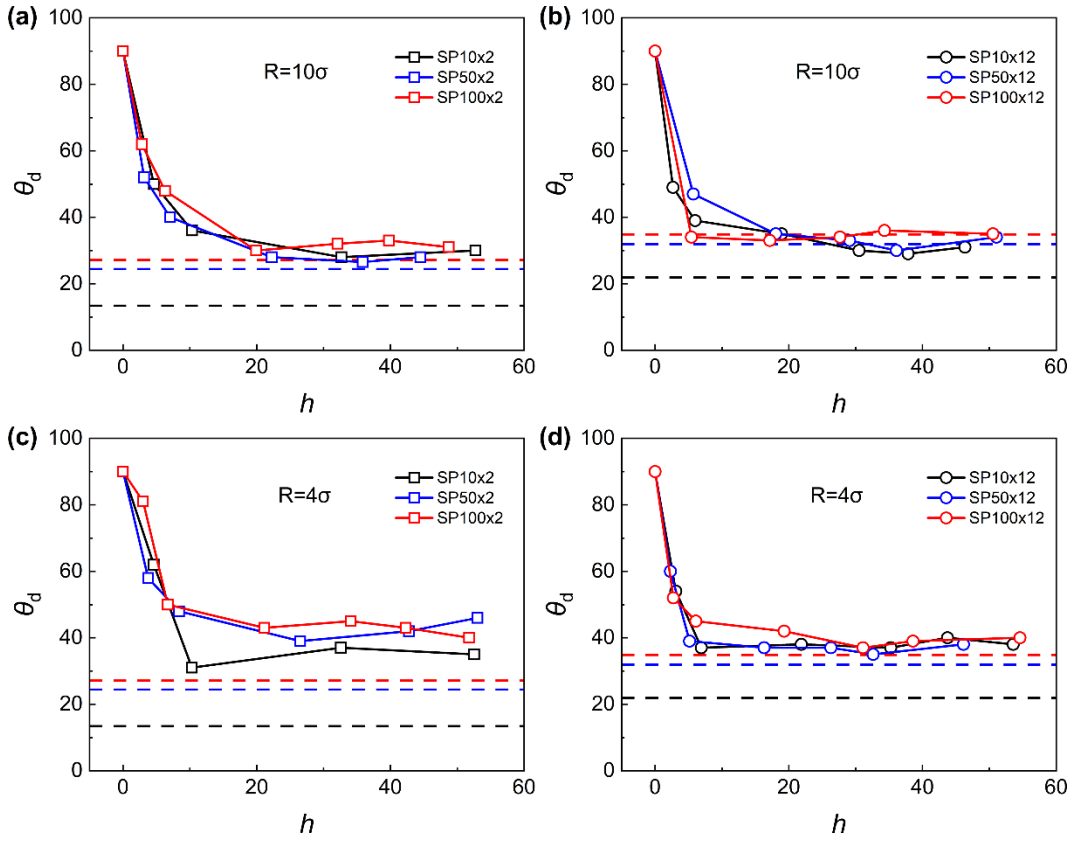

Fig. S1. Variation of the dynamic contact angle θ_d with the wetting height h of both linear polymers and star polymers ($f = 2$ and 12) with different arm length $N_{arm} = 10$ (black), $N_{arm} = 50$ (blue), and $N_{arm} = 100$ (red), in capillaries with different radii (a)(b) $R = 10\,\sigma$ and (c)(d) $R = 4\,\sigma$.

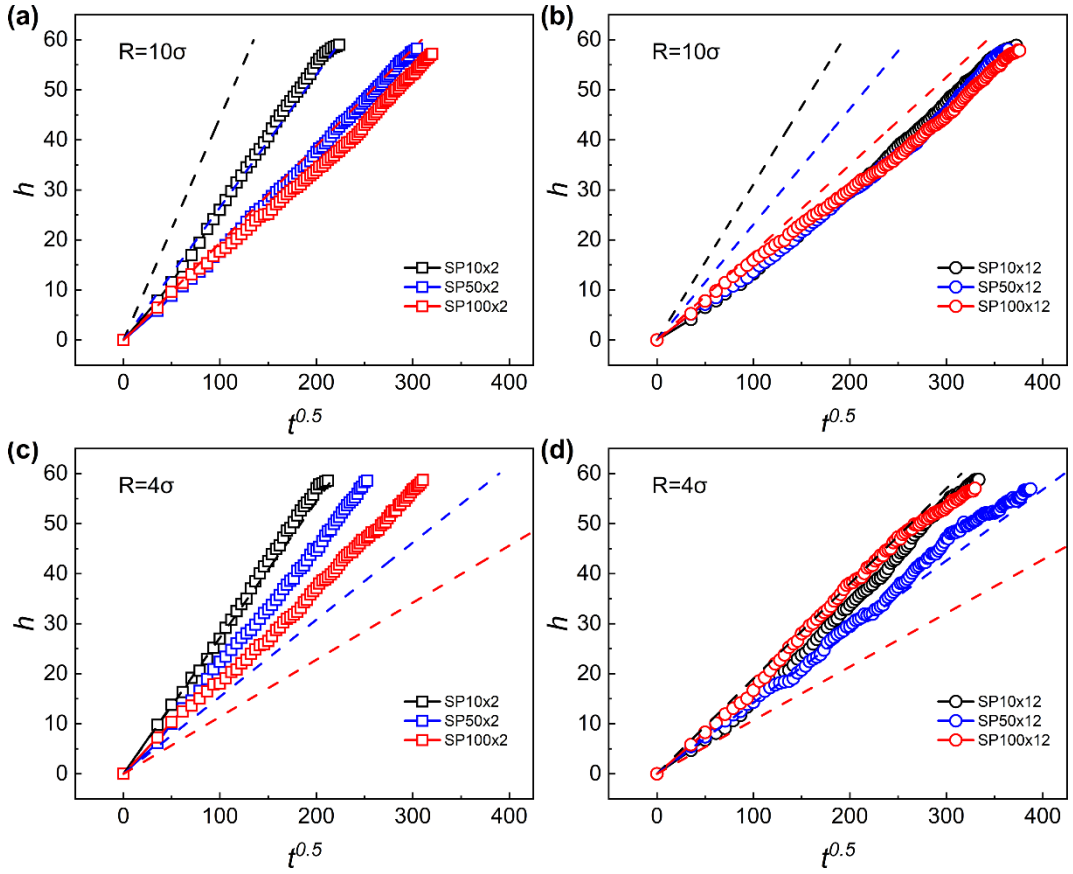

Fig. S2. Comparison of actual capillary filling with the theoretical LWE predictions (modified by dynamic contact angle) for both linear polymers and star polymers ($f = 2$ and 12) with different arm length $N_{arm} = 10$ (black), $N_{arm} = 50$ (blue), and $N_{arm} = 100$ (red), in capillaries with different radii (a)(b) $R = 10\,\sigma$ and (c)(d) $R = 4\,\sigma$.

3. Entanglements

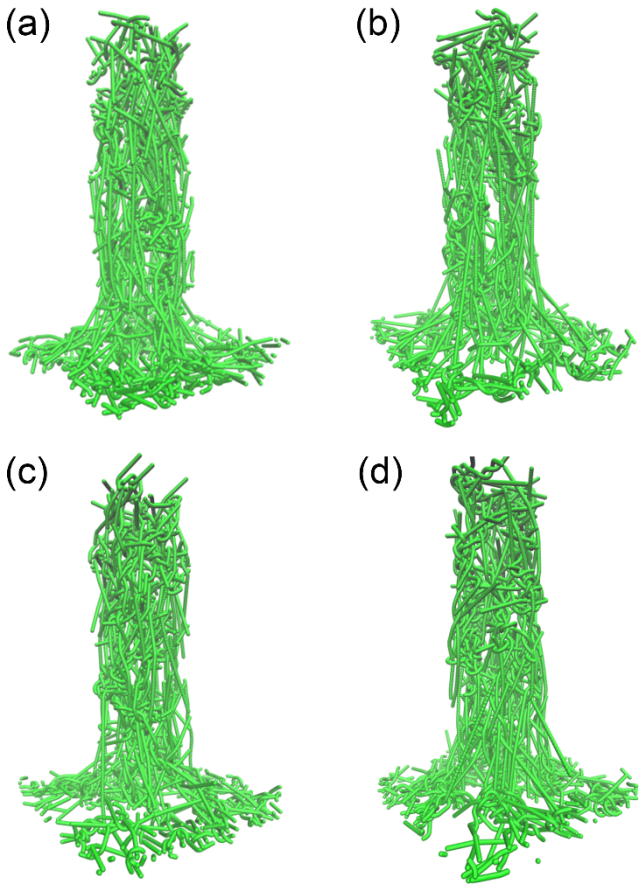

Fig. S3. Snapshots of star polymer topologies after the operation of primitive path analysis algorithm, in the cases of (a) SP100x2, (b) SP100x4, (c) SP100x6, and (d) SP100x12 when $h = 60\,\sigma$ during filling in the capillary of $R = 10\,\sigma$.

4. Distribution of core atoms and end atoms

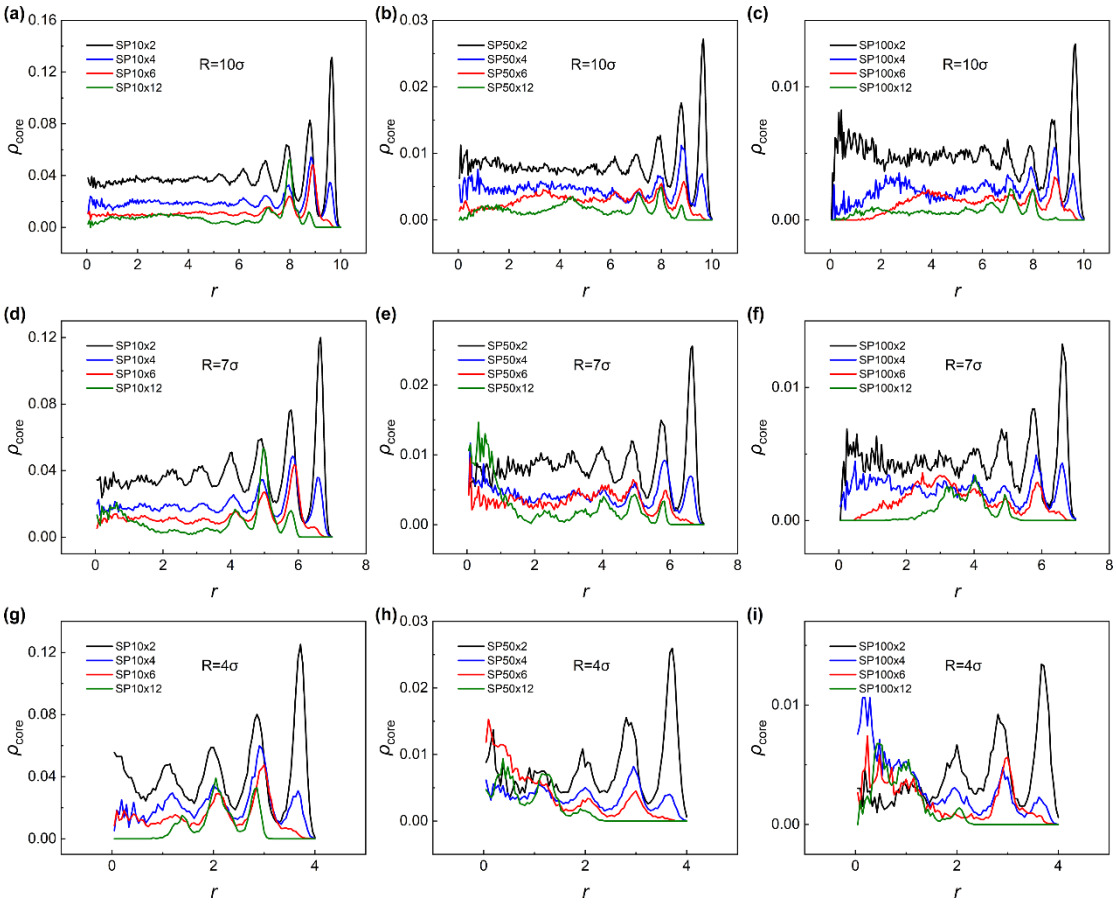

Fig. S4. Variation of the density of core atoms ρ_{core} of different star polymer systems within capillary, with the distance to the central axis r, in the cases of (a) ~ (c) $R = 10\,\sigma$, (d) ~ (f) $R = 7\,\sigma$, and (g) ~ (i) $R = 4\,\sigma$, during imbibition.

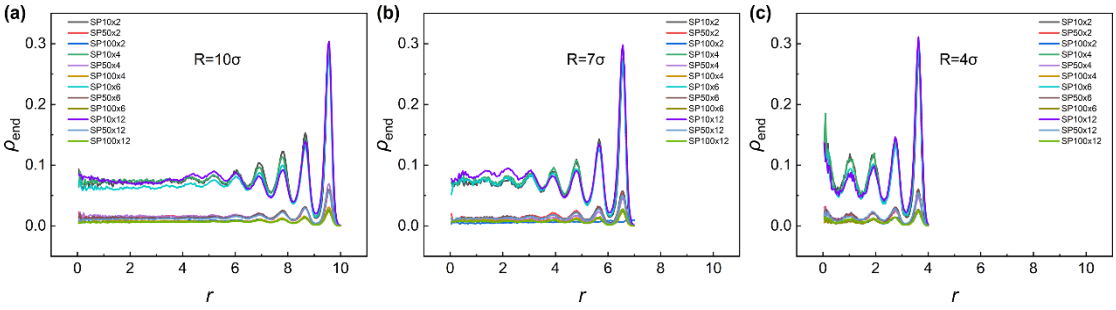

Fig. S5. Variation of the density of end atoms ρ_{end} of different star polymer systems within capillary, with the distance to the central axis r, in the cases of (a) $R = 10\,\sigma$, (b) $R = 7\,\sigma$, and (c) $R = 4\,\sigma$, during imbibition.

5. Chain configurations in the capillary

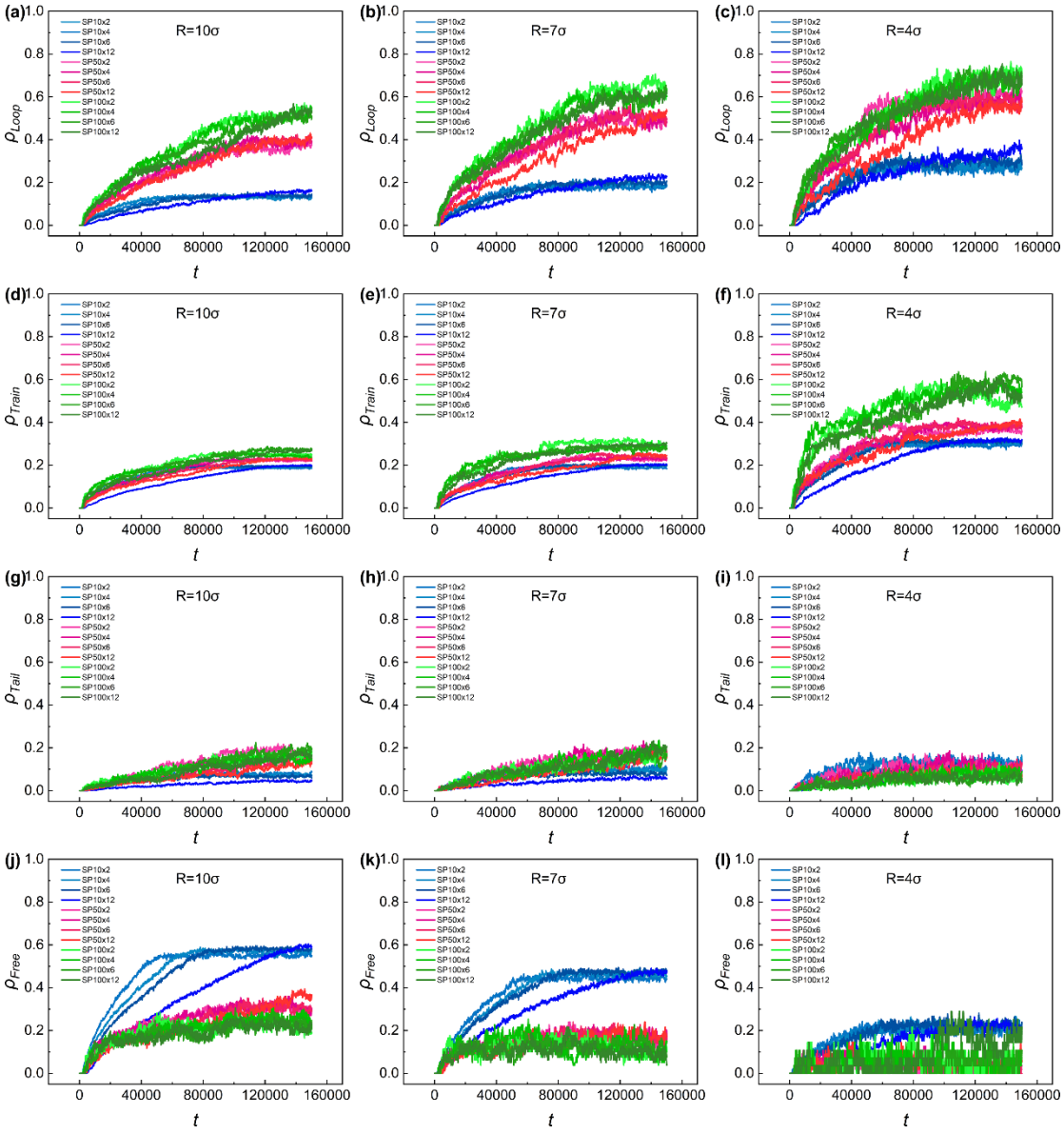

Fig. S6. Variation of the density of adsorbed chains in three types of configurations and free chains with the wetting time t, in the cases of (a) ~ (c) the density of loop ρ_{loop}, (d) ~ (f) the density of train ρ_{train}, (g) ~ (i) the density of tail ρ_{tail}, and (j) ~ (l) the density of free chains ρ_{free}, during imbibition in capillaries of $R = 10\,\sigma$, $R = 7\,\sigma$, and $R = 4\,\sigma$.

6. Self-correlation function of the core-to-end vector

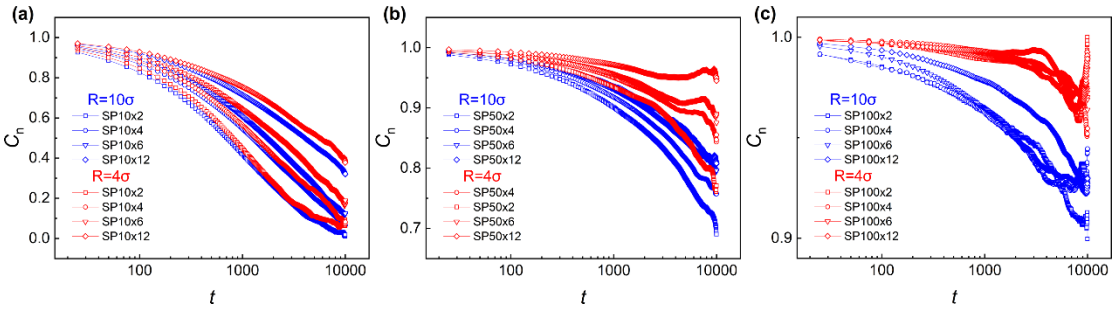

Fig. S7. Comparison of the self-correlation function of the core-to-end vector of the arms C_n in the capillaries of $R = 10\,\sigma$ and $R = 4\,\sigma$, in the cases of systems of (a) $N_{arm} = 10$, (b) $N_{arm} = 50$, and (c) $N_{arm} = 100$.

7. Mean square displacement of core segments.

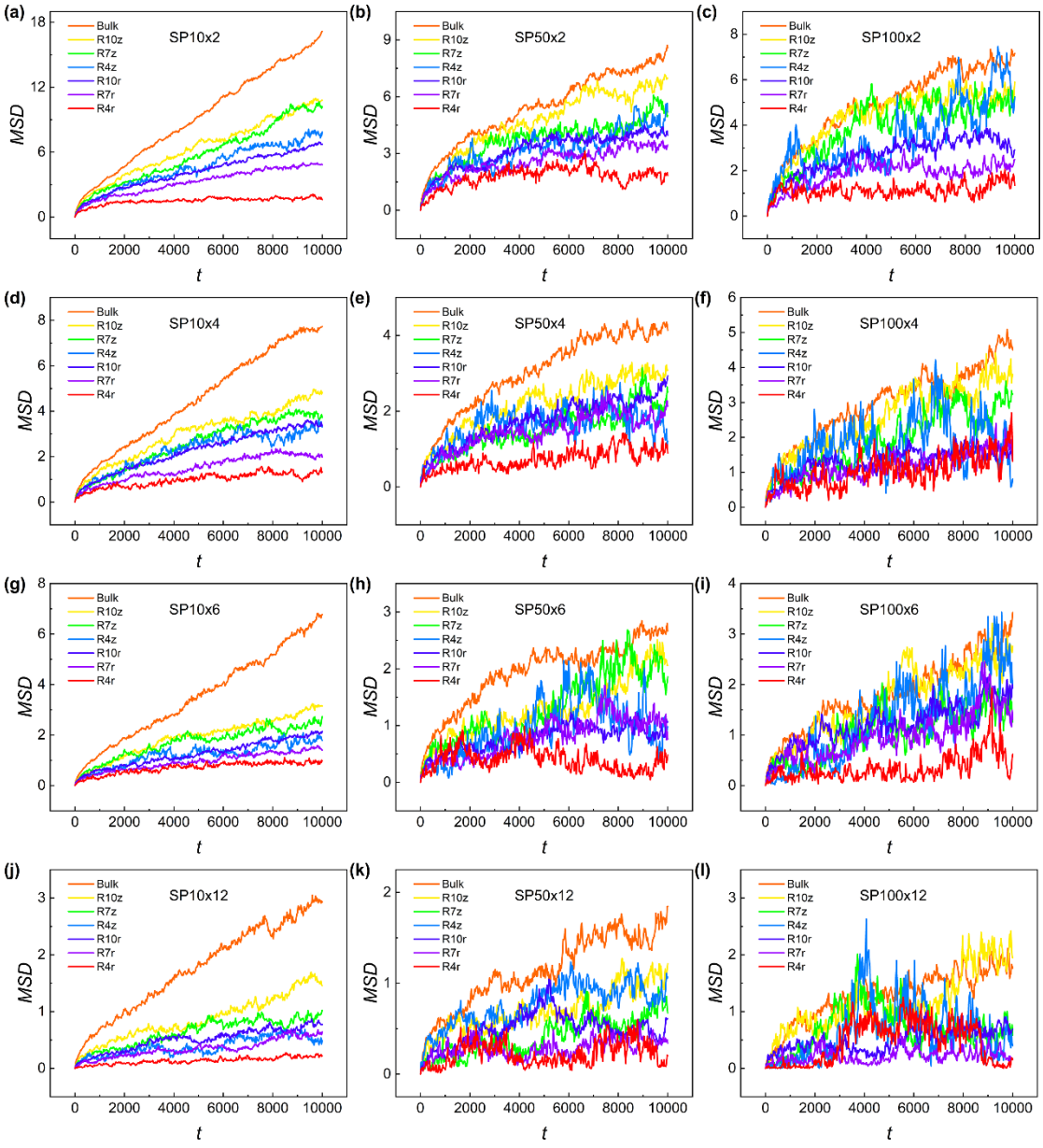

Fig. S8. Comparison of the development of the mean square displacement of core atoms in the radial direction and along the axis of capillary, both under confinement and in the static bulk, in the cases of (a) ~ (c) $f = 2$, (d) ~ (f) $f = 4$, (g) ~ (i) $f = 6$, and (j) ~ (l) $f = 12$. Legends represent the radius of capillary and the direction of displacement where the data were collected. For example, "R10z" stands for the case of MSD along the axis of capillary were collected in the nanopore of $R = 10\,\sigma$.